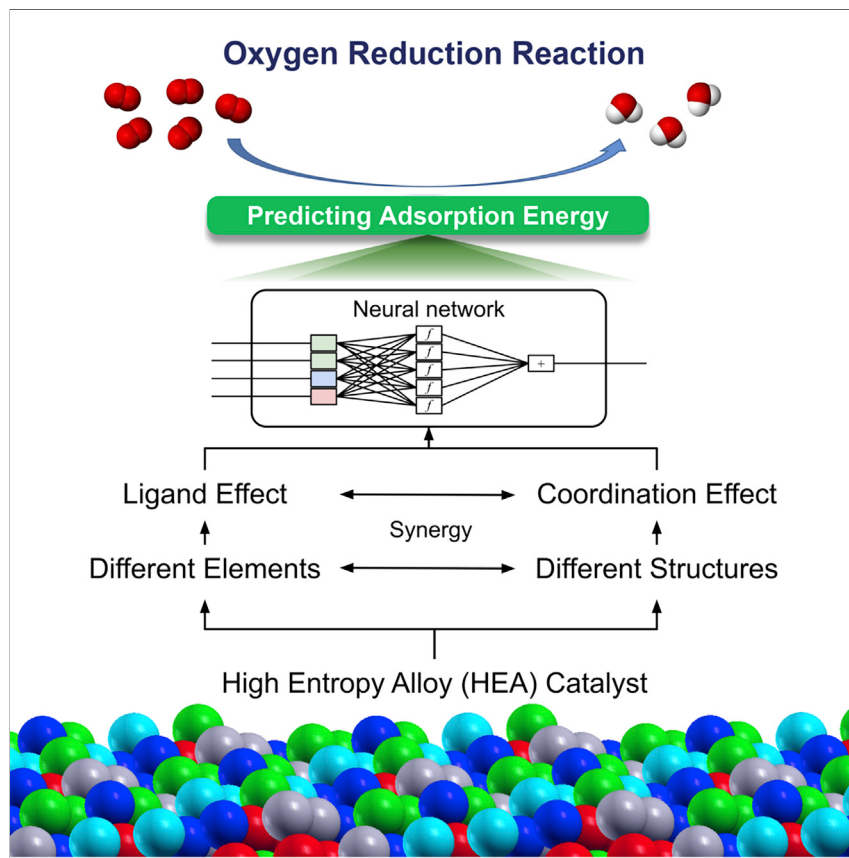


## Article

# Neural Network-Assisted Development of High-Entropy Alloy Catalysts: Decoupling Ligand and Coordination Effects



High-entropy alloys (HEA) provide vast chemical space that can be fine-tuned to create optimal heterogeneous catalysts. We leverage the predictive power of neural network models to accurately predict the adsorption properties of HEA surfaces, simultaneously accounting for different metal elements (ligand effect) and different crystal structures and defects (coordination effect).

Zhuole Lu, Zhi Wen Chen,  
Chandra Veer Singh

chandraveer.singh@utoronto.ca

## HIGHLIGHTS

Neural network accurately predicts catalytic performance of high-entropy alloy

Structure sensitivity of high-entropy alloy is quantified for the first time

Interplay between ligand and coordination effects determines adsorption energy



## Benchmark

First qualification/assessment of material properties and/or performance

Lu et al., Matter 3, 1318–1333  
October 7, 2020 © 2020 Elsevier Inc.  
<https://doi.org/10.1016/j.matt.2020.07.029>



**Article**

# Neural Network-Assisted Development of High-Entropy Alloy Catalysts: Decoupling Ligand and Coordination Effects

Zhuole Lu,<sup>1,3</sup> Zhi Wen Chen,<sup>1,3</sup> and Chandra Veer Singh<sup>1,2,4,\*</sup>

**SUMMARY**

**High-entropy alloys (HEAs) recently emerged as promising catalysts due to their immense chemical space and tunability. However, the large chemical space presents challenges for comprehensive characterization due to experiments' trial-and-error nature. Here, we leverage neural network (NN) and density functional theory to simultaneously account for ligand effect (spatial arrangement of different elements) and coordination effect (different crystal facets and defects) for predicting the adsorption energy. The developed NN model demonstrates three advantages: (1) high accuracy, with a mean absolute error of 0.09 eV; (2) universality, with applicability to bimetallic catalysts; and (3) simplicity, with 36 NN parameters and its further simplification to a linear scaling model at a slight loss of accuracy. Using the trained NN model validated with experimental literature, we decouple the comparative extents of ligand and coordination effects. Our results endow high practical significance and provide important insights for rational design of HEA catalysts.**

**INTRODUCTION**

High-entropy alloys (HEAs) are alloys that consist of many elements, with each element at equimolar ratio or otherwise significant proportion. The high number of element types creates relatively high entropy, which stabilizes the alloy. Originally known for their novel mechanical properties,<sup>1</sup> HEAs recently emerged as a promising and relatively unexplored strategy for fine-tuning catalytic properties due to their large number of active-site types.<sup>2</sup> Because of their tunability, HEAs have been experimentally revealed to be high-performance catalysts for hydrogen evolution reaction (HER),<sup>3</sup> oxygen evolution reaction (OER),<sup>4,5</sup> oxygen reduction reaction (ORR),<sup>6</sup> and ammonia decomposition,<sup>7</sup> all of which are vital chemical reactions in current society with the pressing issues of energy crisis and environmental pollution. In addition, alloying beyond two elements is a robust pathway for balancing catalytic activity and stability.<sup>8</sup>

The enormous number of different types of HEA active sites, however, makes both theoretical and experimental research extremely difficult. Two factors contribute to this large variation in the active sites: random spatial distribution of different metal elements, which we define as "ligand effect,"<sup>9</sup> and the different crystal facets or defects, which we define as "coordination effect."<sup>10</sup> Ligand effect, alternatively known as electronic effect<sup>11</sup> or configurational effect,<sup>12</sup> arises from different surface electronic structures due to the different types of metal in the vicinity of the adsorbate. Coordination effect, on the other hand, describes differences in an adsorbate's coordination with surface metal atoms due to different crystal facets and defects.

**Progress and Potential**

High-entropy alloys (HEAs) are alloys containing typically five or more major elements. Due to their large number of different types of active surface sites, they recently emerged as promising catalysts with the capability of fine-tuning catalytic performance for many important energy-conversion reactions. However, the enormous number of active-site identities makes both theoretical and experimental research extremely difficult. This work leverages machine learning (ML) and density functional theory (DFT) to predict the adsorption energy of key reaction intermediate on HEAs, thereby quantitatively unifying the ligand effect (element identity) and coordination effect (surface structures) for HEA catalysts. Although trained only on DFT data, the ML model's prediction is in general agreement with experimentally measured activity from prior literature, indicating great practical significance of our ML model for designing HEA catalysts.



Coordination effects are known to cause up to 1 eV change in adsorption energy given the same materials composition,<sup>13</sup> which is similar to the range of adsorption energy solely from configurational variations on IrPdPtRhRu HEA,<sup>14</sup> for O\* and OH\*. This suggests that coordination and ligand effects are at the same order of magnitude, and therefore neither effect can be ignored. Additionally, experimentally synthesized HEA catalysts, including nanoparticles (through the carbothermal shock method)<sup>15</sup> and nanoporous samples (through dealloying),<sup>5,6,16</sup> are observed to exhibit a wide range of surface structures; therefore, in-depth theoretical investigations are needed to uncover these complex geometric effects on catalyst activity. HEAs additionally exhibits surface defects, such as vacancy, dislocation, and grain boundary, albeit possessing the same bulk structure (e.g., fcc).<sup>17</sup> A quantitative understanding of ligand-coordination interplay is, therefore, paramount in guiding efforts for shape-, size-, and defect-controlled synthesis of HEAs with excellent catalytic activity.<sup>18</sup>

Furthermore, while conceptually distinct, ligand and coordination effects are almost always entangled together; an active site on HEA has numerous configurational possibilities while it can also present different coordination environments, which is the key for rational design of catalysts. However, to date ligand and coordination effects have only been quantified in isolation, and it remains unclear how the two effects interact with each other and influence the catalytic activity, especially for HEAs. For instance, adsorption energy on the (111) surface of an HEA is found to correlate linearly with the number of neighboring atoms belonging to each metal element,<sup>14</sup> and adsorption energy on monometallic catalysts is found to correlate linearly with the coordination number (CN) on a wide variety of crystal structures and defects,<sup>13,19</sup> but it is unclear how to combine these two methods to predict the adsorption energy on HEAs with different crystal structures and defects and to further design the optimal HEA catalyst.

In the growing chemical space where the structure-property relationship becomes increasingly complex, machine learning (ML) methods have been shown to capture patterns that humans may miss and to effectively search for the desired optimum. This is exemplified by recent ML works on ordered intermetallic alloys,<sup>20</sup> single-atom alloys<sup>21–23</sup> and surface and subsurface alloys,<sup>21,24,25</sup> which represent an extensive effort but are unfortunately restricted to bimetallic alloys. Recently, Batchelor et al. successfully applied ML to an HEA (IrPdPtRhRu) and demonstrated accurate and exhaustive ML prediction of adsorption energies of O\* and OH\*, key descriptors of ORR and OER, only on the (111) surface.<sup>14</sup> However, nanostructured catalysts always endow a large number of low-coordination active sites.<sup>26,27</sup> Therefore, deep insights into the relationships between complex coordination environment and catalytic performance are urgently needed for rational design of high-performance HEA catalysts.

To delineate the competing (or coordinated) role of ligand and coordination on HEA catalyst activity, we develop and train a neural network (NN) model on high-fidelity density functional theory (DFT) calculations. ORR is taken as a model reaction, which plays the central role in fuel cells<sup>28</sup> and metal-air batteries.<sup>29,30</sup> The NN model was used to predict the adsorption energy of OH\* adsorbate, a key ORR intermediate as identified in numerous studies,<sup>31</sup> on five Miller index surfaces and 12 types of coordination environments. The system of IrPdPtRhRu HEA is used as a model catalyst since its constituent elements are well studied in the literature, both experimentally and theoretically,<sup>32</sup> and their atomic radii are close, indicating high likelihood of stability.<sup>14</sup> Combining both configurational and coordination spaces, we are able to

<sup>1</sup>Department of Materials Science and Engineering, University of Toronto, Toronto, ON M5S 3E4, Canada

<sup>2</sup>Department of Mechanical and Industrial Engineering, University of Toronto, Toronto, ON M5S 3G8, Canada

<sup>3</sup>These authors contributed equally

<sup>4</sup>Lead Contact

\*Correspondence:  
[chandraveer.singh@utoronto.ca](mailto:chandraveer.singh@utoronto.ca)

<https://doi.org/10.1016/j.matt.2020.07.029>

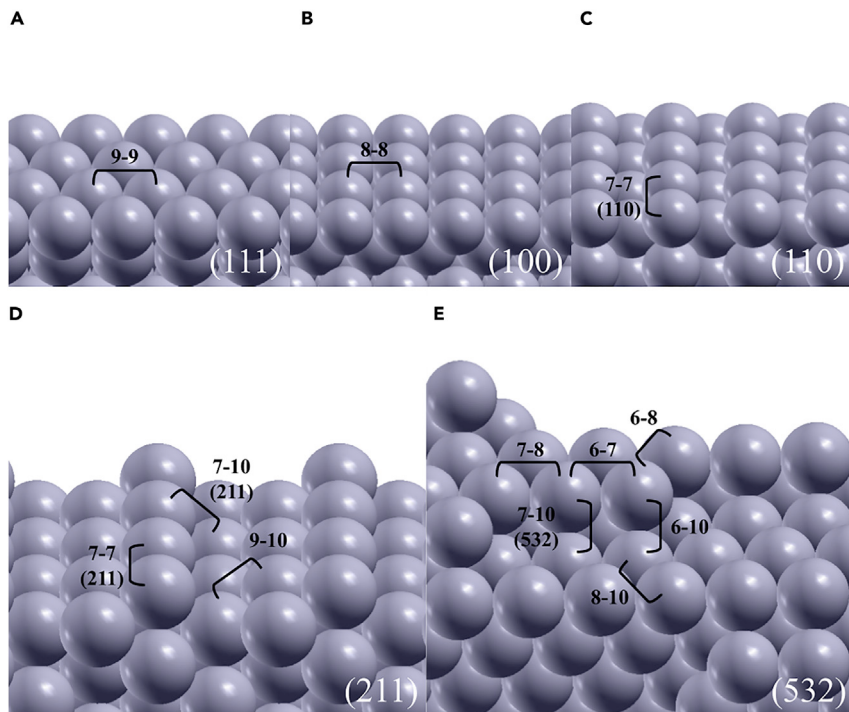


**Figure 1. HEA Surfaces and Active Sites of the Dataset Used for Model Training and Evaluation**

Sites are labeled by their coordination numbers (CN). In cases where the labels appear to be duplicated, the surface indexes are added to distinguish them. Gray balls can be Ir, Pd, Pt, Rh, or Ru. Only bridge sites are included, since on-top and three-fold sites are found to be mostly unstable or unfavorable for OH\* near undercoordinated sites. Numerical CNs are also listed in Table S1.

demonstrate accurate NN prediction on over 1,000 data points. We leverage its prediction power to examine the interplay between ligand and coordination effects and provide insights for future HEA development.

## RESULTS AND DISCUSSION

### Accuracy and Universality of the Developed NN Model

Site-stability analysis revealed that OH\* adsorbate is mostly unstable or unfavorable on on-top and three-fold sites and only stable for bridge sites, consistent with earlier findings showing that OH\* preferentially binds to bridge sites on small clusters of Pt,<sup>33</sup> CuPt,<sup>33</sup> and PtCoNi.<sup>34</sup> Accordingly, different bridge sites were considered for equimolar fcc IrPdPtRhRu HEA surfaces on five commonly observed Miller index surfaces, (111), (100), (110), (211), and (532) (Figure S1), where (111), (211), and (532) surfaces are characteristic of the terrace, edge, and corner of a nanoparticle<sup>35</sup> and are commonly observed. Additionally, (100) and (110) surfaces are low-index surfaces also observed on nanoparticles.<sup>36</sup> The lattice constants are overall close to the bulk lattice constant with less than 3% change. Together, 12 unique coordination environments (Figure 1) were considered in this work. In each coordination environment, the two atoms at each bridge site as well as the neighbors to these two atoms are expected to affect the adsorption energy.<sup>14,37,38</sup> Therefore, in the best scenario, the configurational space includes a minimum of two active-site atoms and nine nearest-neighbor atoms (corresponding to a nanoparticle corner on-top site resembling the 6-7 site in Figure 1E), which gives  $5^{2+9} \approx 5 \times 10^7$  possibilities for

**Table 1. Performance Metrics of NN Model Evaluated with 20 Runs**

Training Set		Testing Set		Metrics on Training Set (eV)		Metrics on Testing Set (eV)	
Description	Size	Description	Size	MAE	RMSE	MAE	RMSE
10% of all data	137	90% of all data	1,233	0.097 ± 0.007	0.119 ± 0.009	0.108 ± 0.009	0.136 ± 0.012
50% of all data	685	50% of all data	685	0.090 ± 0.003	0.114 ± 0.004	0.094 ± 0.007	0.117 ± 0.008
70% of all data	959	30% of all data	411	0.086 ± 0.003	0.108 ± 0.003	0.090 ± 0.004	0.116 ± 0.004
(100) and (211) HEA surfaces	396	(111), (100), and (532) HEA surfaces	781	0.080 ± 0.006	0.101 ± 0.008	0.144 ± 0.025	0.177 ± 0.027
All HEA surfaces	1,177	all bimetallic surfaces	193	0.089 ± 0.003	0.113 ± 0.004	0.092 ± 0.011	0.115 ± 0.011

Values of standard deviation follow “±” signs. MAE and RMSE are mean absolute error and root-mean-squared error, respectively.

a five-element HEA, neglecting symmetry. To conquer this large chemical space, we then resorted to the predictive power of NN.

The model accuracy is demonstrated by an average mean absolute error (MAE) and root-mean-square error (RMSE) of 0.094 eV and 0.117 eV, respectively, on the testing dataset of OH\* adsorption energy, using only 50% of the dataset as the training set (**Table 1**). The achieved level of accuracy is on par with state-of-the-art adsorption prediction models,<sup>39</sup> including convolutional graph neural network<sup>40,41</sup> (MAE: 0.15 eV<sup>42</sup>), atom-centered symmetry functions (ACSF)<sup>43,44</sup> (RMSE: 0.06 eV<sup>37</sup>), and smooth overlap of atomic positions (SOAP)<sup>45–47</sup> (MAE: ~0.12 eV<sup>48</sup>), even though the model in this work is significantly simpler in terms of software implementation as it involves little data pre-processing other than counting CN, unlike aforementioned methods. Using the same 50%/50% training-testing data partition, the parity plot from a typical model training session shows overall agreement between NN-predicted and DFT-calculated adsorption energy values (**Figure 2**), with the vast majority of predicted values falling within ±0.15 eV from the true values. As little as 10% of the dataset, or approximately 140 data points, is sufficient for a comparable MAE of 0.108 eV and an RMSE of 0.136 eV. On the other hand, increasing the training dataset size to 70% of the total data gives an MAE of 0.090 eV and an RMSE of 0.116 eV, showing limited increase in accuracy and indicating that the current NN model has reached its maximum predictive power. Note that the metrics on training and testing datasets are always close, which indicates that no overfitting occurred and is consistent with the compactness of this 36-parameter NN. The high accuracy of our NN model makes the corresponding predicted results trustworthy.

The universality of the NN model is demonstrated by its extrapolation ability. To test whether the current NN model can accurately extrapolate to unseen coordination environments, we trained the NN model on only two surfaces, (100) and (211), and tested its prediction on all other active sites to which the NN model was not exposed beforehand. The NN model achieved a comparable MAE of 0.144 eV and an RMSE of 0.177 eV, only slightly higher than the NN prediction whereby all active sites were included in the training set. This implies that the NN model did not learn the coordination factor as categorical information but rather fully captured the numerical relationship between coordination environment and adsorption energy. This means that the catalytic performance can be predicted by just using the simple CN descriptor rather than the complex surface structures.

To verify whether the NN model can predict for bimetallic catalysts, which can be considered special cases of HEA configurations in terms of NN input, we trained the NN model only on equimolar HEA surfaces and then used it to predict for bimetallic surfaces. The bimetallic dataset covers all five elements involved in the HEA

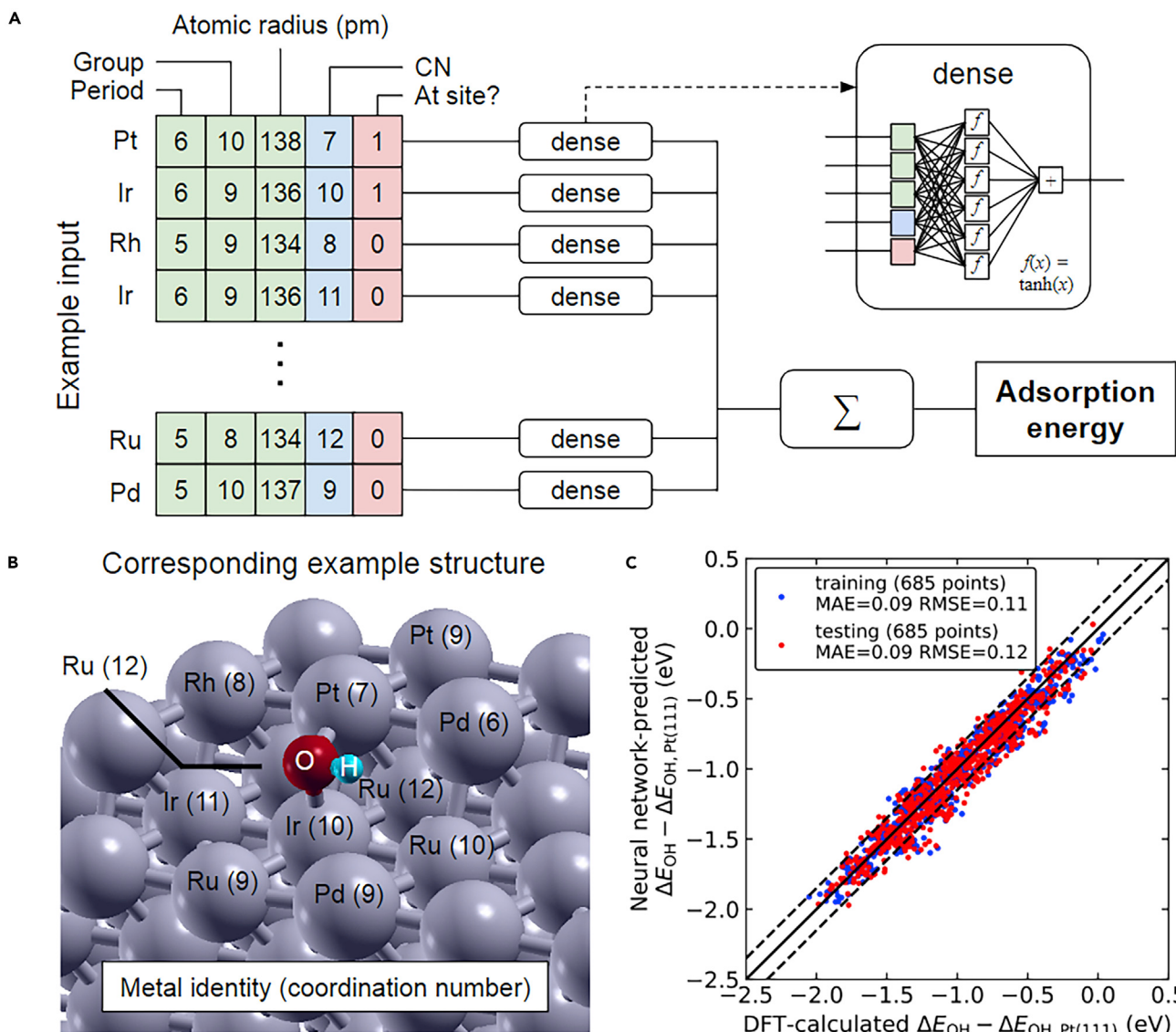


**Figure 2. Machine-Learning Scheme, Example Input Features, and Model Parity Plot**

(A) Input features, their examples (green, blue, and red indicate ligand, coordination, and nearest-neighbor descriptors, respectively), and NN layout, including the dense layers depicted in the inset.

(B) The structure corresponding to the example in Figure 1A, where labeled metal atoms are the active site and its nearest neighbors.

(C) Parity plot and performance metrics following a random data shuffling and a 50%/50% training-testing data splitting. Dotted lines indicate  $\pm 0.15$  eV deviation.

and also spans all five crystal surfaces tested for HEA. The testing MAE and RMSE are 0.092 eV and 0.115 eV, respectively, similar to those of HEAs. This means that the NN model is applicable for both bimetallic and HEA, despite difference in lattice strains, further proving the high universality of our NN model. We also note that throughout all tests there was never overfitting, shown by the consistency between training and testing metrics.

#### Comparison with Existing Experimental Data

Experimentally measured ORR activity can be effectively described by the adsorption energy of  $\text{OH}^*$ ,<sup>31</sup> which is accurately predicted by the developed NN model

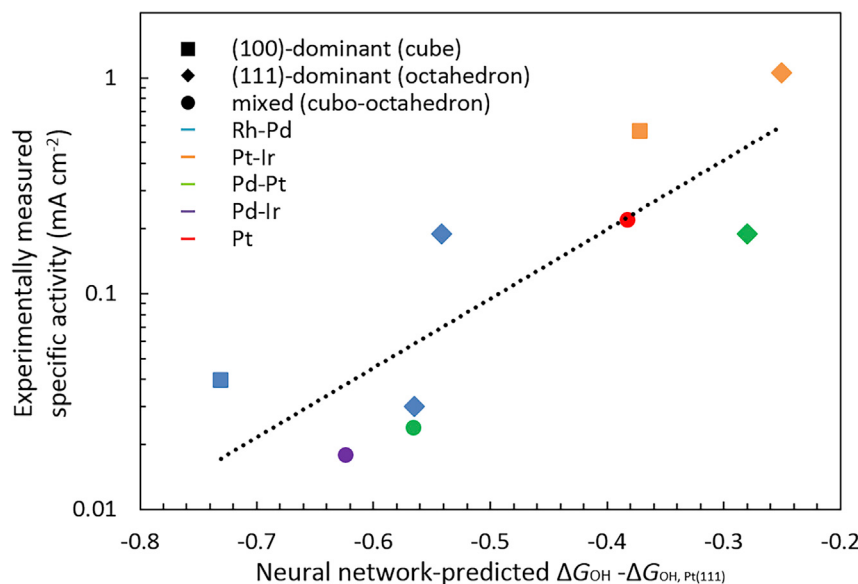


**Figure 3. Comparison between Model-Predicted Adsorption Energy and Experimentally Measured ORR Specific Activity**

Activity measurements were collected from prior studies, all performed at 0.9 V versus reversible hydrogen electrode, with 0.1 M HClO<sub>4</sub>, and at room temperature works (Rh-Pd,<sup>49</sup> Pt-Ir,<sup>50</sup> Pd-Pt,<sup>51,52</sup> Pd-Ir,<sup>53</sup> and Pt<sup>50,51</sup>). Most referenced studies utilized precise shape-controlled synthesis and therefore enable comparison of coordination effect. Some studies included several different metal molar ratios, therefore giving more than one data point. Dotted line is added to guide the eye. More details are found in section 6 of *Supplemental Information*.

as shown in the previous section. We validate its experimental accuracy by comparing experimentally measured ORR specific activity from prior literature with corresponding model-predicted OH\* adsorption energy (Figure 3). Only works with precise control over the shape and surface structure of catalysts are included, so that the NN can be input with the exact coordination information and that its experimental accuracy can be evaluated with regard to coordination effect. Previous studies<sup>49–53</sup> succeeded in synthesizing two categories of shapes: cube and octahedron. Cubes expose a high ratio of (100) surfaces while octahedra expose (111) surfaces predominantly, both of which were verified with electron microscopy techniques in the respective works.<sup>49–51</sup> Note that because HEA catalysis is still in its infancy and few HEA catalysts have been reported for ORR, we are limited to comparison with only bimetallic catalysts. Nevertheless, as discussed in the previous section, bimetallic catalysts are treated as special cases of HEA catalysts and therefore can be equally used in experimental validation.

Despite the challenges in bridging the theory-experiment gap, general agreement is found between experimentally measured specific activity and the NN-predicted adsorption energy, as shown in Figure 3. The ORR activity generally increases with weaker OH\* adsorption, since these data points lie to the left of the ORR volcano tip<sup>31</sup> and therefore weaker OH\* adsorption gives higher overpotential. The inclusion of both different elements and facets indicates that the developed NN model is experimentally accurate with regard to both ligand and coordination effects. On the other hand, other factors that have not been considered by the NN model could influence ORR activity. For instance, strain effect has also been shown to affect the activity.<sup>54,55</sup> Strain effect is less of a concern for well-matched lattices, as in the case of bimetallic and HEA studied here, but could be more pronounced for atoms

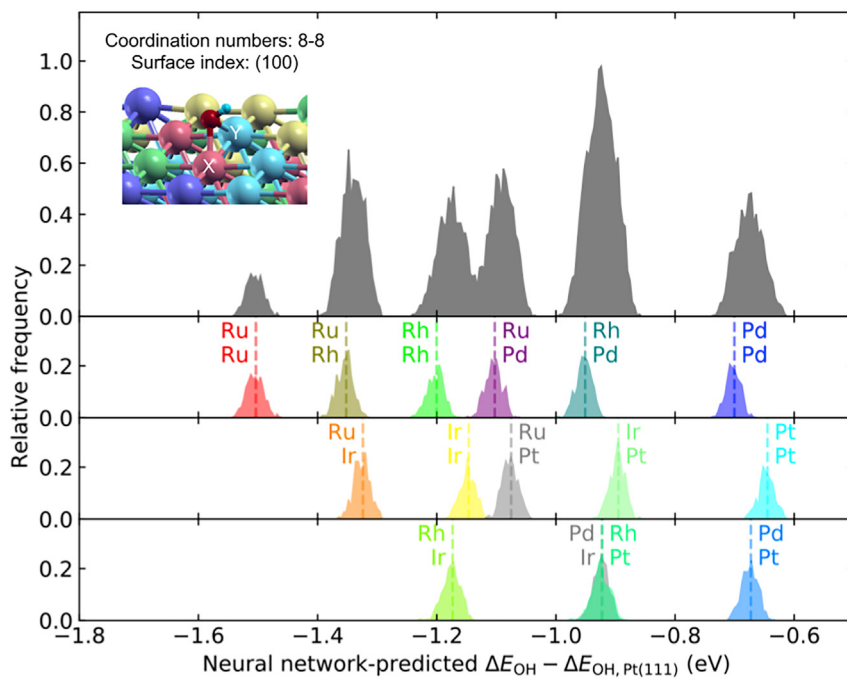


**Figure 4. Frequency Distribution of OH\* Adsorption Energy Resulting from Ligand Effect (Random Distribution of HEA Elements) Using the (100) Surface as an Example**

The top row shows the overall energy distribution, which is broken down in terms of the identity of the two active-site atoms, marked as X and Y in the inset, shown in the bottom three rows. The bottom three rows are used to separate peaks that are otherwise overlapping. Dotted lines indicate the average values of the corresponding peaks.

with drastically different radii, where phase segregation occurs and one phase stretches or compresses the neighboring phase, as in the case in certain core-shell structures. Secondly, some suggest that other anions in alkaline electrolytes could compete with OH\* adsorption, influencing ORR activity.<sup>56,57</sup> In this case, the same NN architecture could be used to additionally predict the adsorption of other anions, from which a higher-level, microkinetics model can be formed.

The NN model predicts weaker adsorption for the higher-coordinated (111) than the lower-coordinated (100), and the experimental activity values also generally agree, with higher activity on (111) than on (100) when given the same composition and molar ratio. Such coordination sensitivity is of particular importance when one considers catalysts with identical elements and molar ratio give different ORR activity due to different abundance of facet types. Therefore, a closer look into the quantitative interplay between ligand and coordination effects is needed, which is discussed in the next section.

### Ligand Effect

The high accuracy of the NN model empowers us to reliably sample the vast configurational space instantly, thereby understanding how different HEA elements contribute to the binding strength. Here, the ligand effect was first investigated in isolation before combining with coordination effect. We used the bridge site on (100) surface as an example and generated 10,000 instances of randomly shuffled element positions while fixing the (100) lattice points and the equimolar ratio. These element positions were fed into the fully trained NN as the input, and the output was collected instantly (Figure 4).

The frequency distribution of OH\* adsorption energy is continuous, indicating that the catalytic activity of HEA can be fine-tuned to target a desired value. The frequency distribution also possesses distinct peaks, and to understand their physical origin we classified each data point in terms of the identity of the two active-site atoms, thereby decomposing the frequency distribution. We found that the decomposed peaks are all similar in width and shape, with distinct centers. For active sites with identical elements, X-X, the average adsorption energy follows the order Ru-Ru < Rh-Rh < Ir-Ir < Pd-Pd < Pt-Pt, which is in complete agreement with the trend in monometallic catalysts, Ru < Rh < Ir < Pd < Pt.<sup>32</sup> Additionally, for active sites with different elements, X-Y, the adsorption energy lies at the average of X-X and Y-Y. For instance, Ru-Rh centers at the middle of Ru-Ru and Rh-Rh. This suggests that the adsorption energy is determined by mixing the contributions from individual elements. These patterns also indicate that the two active-site atoms, being directly bonded to OH\*, are the dominant factor in determining the adsorption energy. The additional fluctuations of around  $\pm 0.1$  eV are likely due to a combination of nearest-neighbor effect and random noise in training data (due to finite chemical accuracy of DFT). Nearest-neighbor effect will be further clarified in the next section.

### Coordination Effect

Ligand and coordination effects were further decoupled by varying each factor independently and observing the corresponding changes in adsorption energy. Using the NN model fully trained on all available data, 10,000 equimolar HEA surfaces were generated for each coordination environment and prediction was made on all generated surfaces, effectively repeating the procedure in the previous section for different coordination environments (Figure 5A). The resulting adsorption energy values on HEA surfaces form continuous distributions similar to that found in the previous section, and also result from superimposing smaller peaks (Figure 5B, left).

Despite the difference in shape, the means of adsorption energy frequency distributions are linearly correlated with the degree of coordination, which can be quantified using total CN of nearest neighbors

$$\overline{CN}_{\text{neighbours}} = \sum_i^{\text{nearest neighbours}} \frac{CN_i}{CN_{\max}},$$

where CN<sub>max</sub> is the maximum possible CN and is 12 for fcc (Figure 5B, middle). On the (111) surface, the upper end of the HEA adsorption energy range is approximately 0.2 eV lower than on the pure Pt(111) surface. This implies that, even though Pt is a constituent element of this HEA, all (111) sites bind OH\* more strongly than pure Pt(111), which is consistent with the equimolar restriction and, as a result, absence of pure Pt(111) in the distribution. Tuning the composition away from equimolar ratio may lead to adsorption energy closer to the peak of the ORR volcano plot ( $\sim 0.1$  eV weaker adsorption energy than pure Pt<sup>31</sup>).

Structure-induced shifting of adsorption energy, with lower-coordinated environments having stronger OH\* binding, is consistent with the structure-activity relation on monometallic catalysts<sup>58</sup> and with earlier findings discussed in the experimental comparison section. In addition to active-site CNs, the nearest-neighbor CNs also contribute to the adsorption energy, albeit to a lesser extent, which could be the key to tuning for the optimal catalytic performance.<sup>58</sup> In particular, active sites with identical CNs but different nearest-neighbor CNs, such as 7-7 (110) and 7-7 (211), are centered at 0.1 eV apart. Previously, for monometallic catalysts, the need for distinguishing beyond the first nearest neighbor motivated the

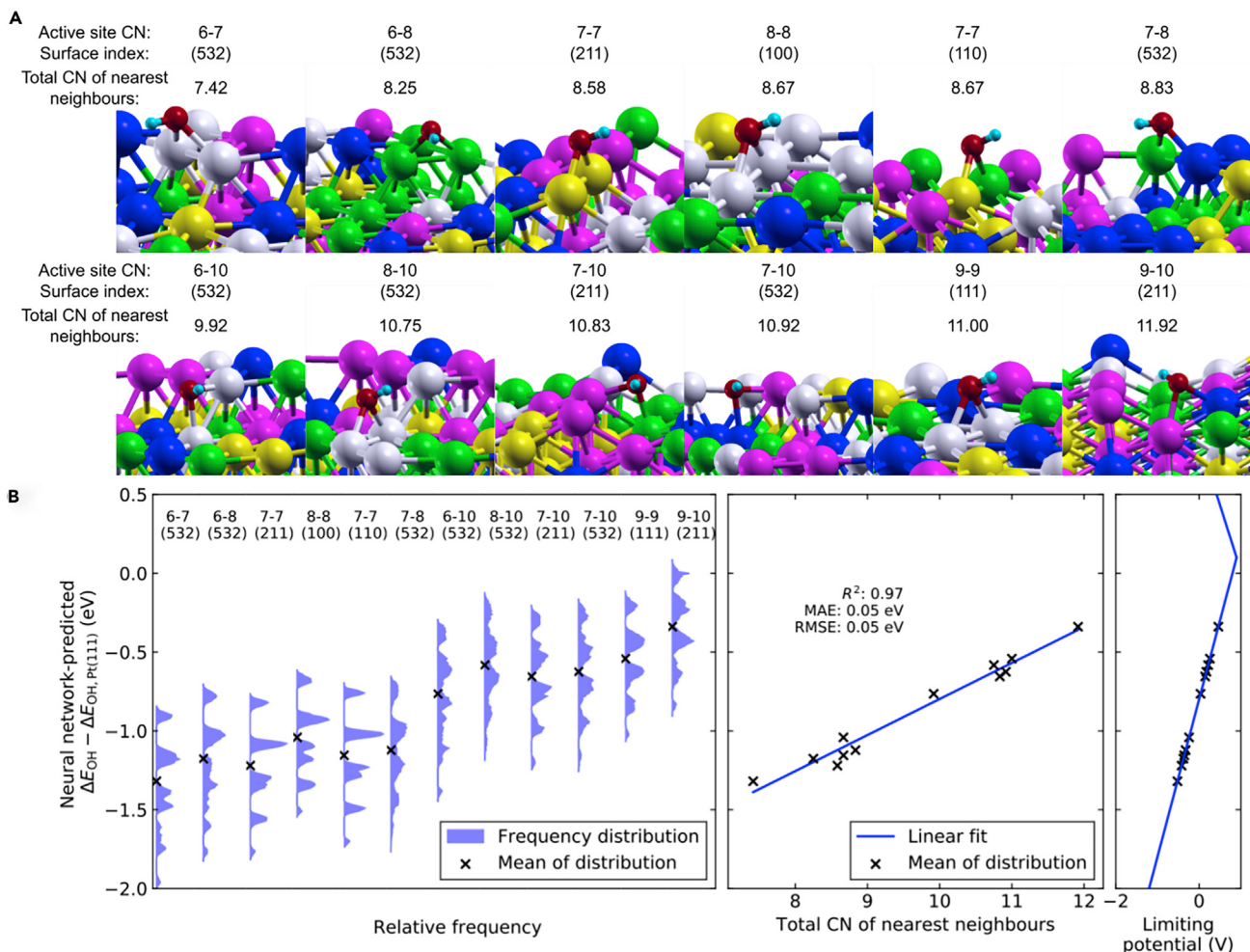


**Figure 5. Adsorption Energy Affected by Combined Ligand and Coordination Effects**

(A) Different coordination environments are ranked in increasing order of total coordination number of nearest neighbors, defined in the text. (B) Frequency distribution of OH\* adsorption energy for each coordination environment (left), whose mean values are found to correlate linearly with the total coordination number of nearest neighbors (middle). The correspondence to overall limiting potential,  $U_L$ , is calculated based on methods in *Supplemental Information* section 5 (right).<sup>31</sup>

The coordination types are ordered the same way in (A) and (B), and the energy values are horizontally lined up in (B).

development of the generalized CN method.<sup>19</sup> It is noteworthy that most coordination environments studied in this work are undercoordinated ones, bind to OH\* more strongly, and therefore have lower limiting potential; the only overcoordinated site in the dataset is 9-10 (211), located in the valley of (211) surface, and exhibits higher average adsorption energy than normal coordinated sites on (111) (Figure 5B, right). The higher end of the adsorption energy range even reaches beyond pure Pt(111) and toward the ORR volcano peak.<sup>31</sup> An important strategy for achieving higher activity ORR catalyst is, accordingly, to create higher-coordinated sites, such as cavities<sup>58</sup> and concave nanoparticles<sup>59</sup> from the monometallic counterparts.

#### Contribution of Individual HEA Atoms to Adsorption

Leveraging the NN design (Figure 2A), the contribution of each HEA atom to the final OH\* adsorption energy was broken down by varying the input to the isolated dense layer component and observing its output without summation over all atoms

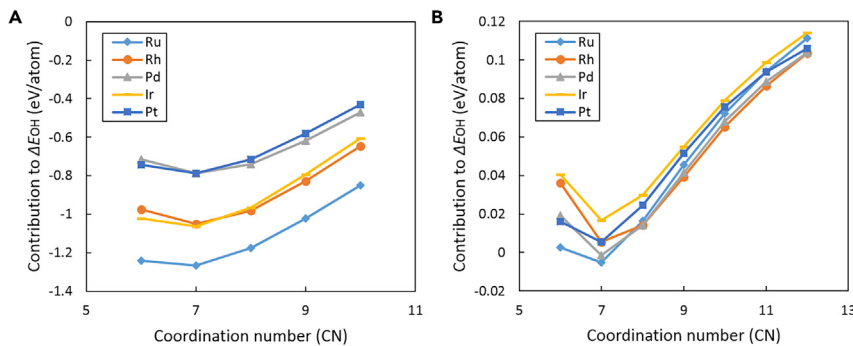


**Figure 6. Contribution of Individual HEA Atoms to Adsorption**

Contribution to OH\* adsorption energy by individual active-site atom (A) and nearest-neighbor atom (B), calculated using the trained NN component depicted in the inset of Figure 2A.

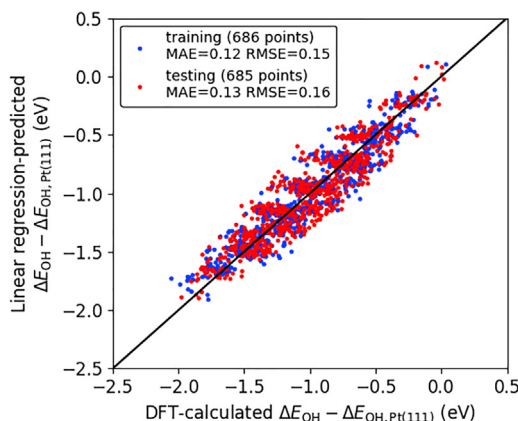
(Figure 6). Each active-site atom contributes to the final adsorption energy at the order of 1 eV/atom, one order of magnitude higher than that from nearest-neighbor atoms, at less than 0.1 eV/atom. On the other hand, there are many more nearest neighbors (10–15) than active-site atoms (only two), and thus their collective contributions are comparable.

Adsorption energy is correlated with the element identities, but more strongly for active-site atoms than for nearest neighbors. For nearest neighbors, the variations due to element identities are at 0.02 eV, which are much lower than variations due to CN, which are at 0.12 eV. During NN training, such low insensitivity in element (compared with CN) could probably prevent us from finding the precise element correlation for nearest neighbors due to stochasticity. It also indicates that, for nearest neighbors, element identity may not be an important factor compared with CN in determining the adsorption energy, at least for equimolar HEAs. This suggests a way in which HEA catalytic activity can be tuned by creating different coordination environments via nanostructure synthesis strategies.

Consistent with findings from previous sections, higher CN generally weakens adsorbate binding strength for both active-site atoms and nearest neighbors. The exception is at CN of 6, which could arise from lattice distortion associated with the corner-like structure. Interestingly, nearest neighbors have mostly positive contribution to adsorption energy. If an atom is added to the site as a nearest neighbor, its positive contribution would weaken the adsorption energy, but at the same time one or both active-site atoms experience an increase in CN, further weakening the adsorption energy. On the other hand, this would imply that these atom-wise contributions should not be interpreted strictly on the basis of their absolute magnitude, as an increase in adsorption energy can be assigned either to an increase in the active-site CNs or to the addition of a new nearest neighbor, or both. Rather, it is the relative energy contribution (with respect to a fixed CN) that is worth noting.

#### Simplifying Ligand-Coordination Interaction Using a Linear Model

In addition to accuracy and universality, the NN model was developed with a third goal, simplicity, whereby the NN model had a minimal design with only one layer and 36 parameters. This philosophy led us to additionally consider the possibility of further simplifying the current NN model to a linear scaling model, which could potentially afford us an intuitive and convenient method for predicting adsorption

**Figure 7. Linear Regression****Prediction of OH\* Adsorption Energies**

The NN model could be simplified to a linear scaling model at a slight loss of accuracy.

energy. According to observations based on the trained NN model, the following equation was assumed:

$$\Delta E_{\text{OH}} - \Delta E_{\text{OH}, \text{Pt}(111)} = E_0 + \sum_i^{\text{all active site atoms}} a_{\text{element}(i)} \text{CN}_i + \sum_i^{\text{all nearest neighbours}} b_{\text{element}(i)} \text{CN}_i,$$

and least-squares fitting was performed on all available data, where  $\text{CN}_i$  is the CN of the  $i$ th atom, and  $E_0$ ,  $a_{\text{element}(i)}$ , and  $b_{\text{element}(i)}$  are parameters to be fitted (element( $i$ ) refers to the element identity of  $i$ th atom and therefore there are  $a_{\text{Pt}}$ ,  $a_{\text{Pd}}$ , ...  $b_{\text{Ru}}$ ,  $b_{\text{Ir}}$  to be fitted). In this simplified model, the contribution of each atom to the adsorption energy is weighted by both its CN and a factor specific to its elemental identity and its proximity to adsorbate (i.e., at active site or nearest neighbor). After performing least-squares fitting using the same 50%/50% training/testing dataset split as in NN training, the testing MAE and RMSE are 0.13 eV and 0.16 eV, respectively, slightly higher than those from NN, which are 0.09 eV and 0.12 eV, respectively. The predicted and DFT-calculated lie reasonably close (Figure 7) but are further apart compared with that from NN in Figure 2C.

The fitted parameters in the linear regression model (Table 2) are consistent with the findings in the NN model in a number of ways. The order, Ru < Rh < Ir < Pd < Pt, is preserved for active-site atoms, but no clear elemental order exists in nearest neighbors due to the lesser influence of nearest neighbors on adsorption energy. This is also verified by the smaller magnitudes of  $b_i$  compared with  $a_i$ . The linear equation also rationalizes the earlier finding where the adsorption energy at site X-Y takes the average value of X-X and Y-Y. Finally, the reasonable accuracy of this 10-parameter linear regression model explains why a mere 36-parameter NN model can perform so accurately.

By sacrificing some accuracy, we are able to achieve more simplicity. By the same token, it is possible to increase accuracy in the current model by incorporating a more sophisticated descriptor, such as the crystal graph convolutional NN,<sup>40</sup> which necessarily requires more hyperparameter tuning.

## Conclusions

In this study, we leveraged the predictive power of NN modeling to understand the interplay between ligand and coordination effects on catalytic performance. The NN model can predict for OH\* adsorption energy, a key ORR descriptor, on IrPdPtRhRu HEA catalyst with random element distributions and 12 unique coordination environments. The NN model possesses three key advantages: (1) high accuracy,

**Table 2. Fitted Parameters in Linear Regression Model (Values in eV)**

Metal Identity of <i>i</i> th Atom element( <i>i</i> )	Intercept $E_0$	Active-Site Atoms $a_{\text{element}(i)}$	Nearest Neighbors $b_{\text{element}(i)}$
Ru	-3.416	0.425	0.157
Rh		0.732	0.145
Pd		1.070	0.140
Ir		0.753	0.165
Pt		1.109	0.141

whereby the testing set MAE and RMSE reached 0.09 eV and 0.12 eV, respectively, using only 50% of the dataset; (2) high universality, whereby similar MAE and RMSE are achieved also on bimetallic catalysts; and (3) simplicity, whereby the model only requires 36 parameters and further simplification to a linear scaling model is possible. The model prediction was compared with prior experimental literature and was shown to be in general agreement with experimentally measured ORR activity values. Using this high-fidelity NN model, we predict for many configuration-coordination combinations that are impractical to be calculated by DFT or measured in experiments. Ligand and coordination effects were then decoupled, revealing that more undercoordinated sites bind to OH\* more strongly, in agreement with previous experimental findings. On a quantitative level, it is found that the adsorption energy is approximately linear in the total CN of nearest neighbors. The NN model additionally aided deconvoluting contributions to the adsorption energy from individual metal atoms near the active site, quantifying the exact influence from element identity, CN, and neighbor nearness. Finally, the NN model can be simplified to a simple linear scaling relationship at the cost of slight accuracy loss. By utilizing the recently developed NN techniques, we demonstrated its power and future use in conquering the vast chemical space due to the configurational and structural degrees of freedom in HEA catalysts.

## EXPERIMENTAL PROCEDURES

### Resource Availability

#### Lead Contact

Further information and requests for the dataset and/or code should be directed to and will be fulfilled by the Lead Contact, Prof. Chandra Veer Singh ([chandaveer.singh@utoronto.ca](mailto:chandaveer.singh@utoronto.ca)).

#### Materials Availability

This study did not generate any reagents.

#### Data and Code Availability

The HEA dataset has been extracted into table format consisting of element identity and corresponding adsorption energy, which is available in [Supplemental Information](#) as a .csv file ([Table S2](#)) as well as the online repository. The NN code has also been made available in the repository. This repository is hosted at [github.com](https://github.com/jol-jol/neural-network-design-of-HEA) and can be publicly accessed at <https://github.com/jol-jol/neural-network-design-of-HEA>, with instructions on how to access the NN architecture as well as reproducing figures in this work.

### DFT Calculations

Spin-polarized plane-wave DFT calculations were conducted with the software package VASP,<sup>60</sup> using the projector augmented wavefunctions<sup>61</sup> and the Perdew-Burke-Ernzerhof exchange functional.<sup>62</sup> For DFT computations, the kinetic energy cutoff for

the wave function calculations was set at 500 eV. Fermi smearing function was used with a smearing width of 0.1 eV to facilitate the DFT convergence. To check for effect of van der Waals (vdW) interaction, which has been shown to affect adsorption calculations,<sup>63,64</sup> we tested a randomly selected subset of the dataset using Grimme's DFT-D3 method,<sup>65</sup> from which negligible differences were found (for a detailed discussion, see [Supplemental Information](#) section 7 and [Figure S3](#)), and accordingly vdW correction was not used for generating the dataset. Supercell contained at least 64 atoms. The Monkhorst-Pack scheme with (2,2,1) k-points was employed. Geometry relaxation was stopped when no force on each atom exceeded 0.02 eV/Å.

To understand the role of surface facets, we created different Miller index surfaces with help from Atomic Simulation Environment<sup>66</sup> and the Python package PyMatGen.<sup>67</sup> Lattice constant was taken as the average of those of five elements in their monometallic form, in accordance with the Vegard's law. To avoid periodic image interaction in the lateral directions, all surfaces are created such that the lateral dimensions are at least 10 Å. For all surfaces at least four atomic layers were included, and the bottom two layers were fixed during geometric relaxation. In the vertical direction, a vacuum of at least 10 Å was also added.

The adsorption energy of OH\* was calculated as

$$\Delta E_{\text{OH}} = E_{\text{OH}*} + 0.5E_{\text{H}_2} - E_* - E_{\text{H}_2\text{O}}, \quad (\text{Equation 1})$$

where  $E_{\text{OH}*}$ ,  $E_{\text{O}*}$ ,  $E_*$ ,  $E_{\text{H}_2}$ , and  $E_{\text{H}_2\text{O}}$  are the electronic energies of OH\*-adsorbed surface, O\*-adsorbed surface, clean surface, H<sub>2</sub> molecule, and H<sub>2</sub>O molecule, respectively. When compared with a reference material, such as the most referenced Pt(111), H<sub>2</sub> and H<sub>2</sub>O energies cancel out,

$$\Delta E_{\text{OH}} - \Delta E_{\text{OH}, \text{Pt}(111)} = (E_{\text{OH}*} - E_*) - (E_{\text{OH}*, \text{Pt}(111)} - E_{*, \text{Pt}(111)}), \quad (\text{Equation 2})$$

which is a convenient form and is therefore used throughout this work. Methods for conversion from  $\Delta E$  to  $\Delta G$ , Gibbs free energy, are described in section 5 of [Supplemental Information](#) and are used to calculate for the theoretical overpotential in [Figure 5](#).

### ML Feature Engineering

While developing the NN model, the coordination factors of the HEA active sites were described in this work using CN, defined as the number of neighbor metal atoms bonded to each atom. Although the CN and generalized CN methods yielded high accuracy in predicting adsorption energy for monometallic<sup>13,19,20</sup> and limitedly bimetallic catalysts,<sup>68</sup> it is not intuitive how it can be adapted to HEAs where the configurational space is orders-of-magnitude larger. While other novel structural descriptors<sup>48</sup> were recently developed successfully, such as SOAP,<sup>45-47</sup> ACSF,<sup>37,43,44</sup> and crystal graph convolutional neural network (CGCNN),<sup>40,41,42</sup> it is desirable to use the CN method, as it is a long-established concept and is likely most intuitive to the catalysis field. In particular, ACSF and CGCNN are methods for general structures, while HEAs possess fixed structures, most commonly fcc and bcc.<sup>69</sup> Using ACSF and CGCNN for HEA would be, therefore, sufficient but probably not necessary. On the other hand, SOAP is a measure that compares between two chemical environments and is therefore suited for kernel-based ML methods exclusively. To describe the ligand effect, we use period number, group number, and experimentally measured metallic atomic radii, based on prior findings.<sup>22</sup> In addition to coordination and ligand descriptors, a third descriptor indicates whether the metal atom is part of the active site or the nearest neighbor to the active site. The combination of the ligand and coordination is a highlight of the novelty of this work.

### Neural Network Models

The NN prediction for the entire HEA site is realized by summing the individual contributions from each metal atom near the adsorbate, similar to the approach taken in the ACSF method.<sup>37,43,44</sup> For each metal atom, the ligand, coordination, and nearest-neighbor descriptors are concatenated into a descriptor vector, and descriptor vectors from all atoms in a given DFT calculation are joined into a matrix, forming one sample input (Figure 1A, left). The individual contribution from each metal atom is calculated by passing its descriptor vector to a 6-node dense NN layer (Figure 1A, inset). The final adsorption energy is then summed using a reduce-sum layer. Overall, it is calculated as

$$y = \sum_i y_i = \sum_i A_2 f(A_1 \vec{v}_i), \quad (\text{Equation 3})$$

where  $\vec{v}_i$  is the 5-dimensional descriptor vector of the  $i$ th atom,  $A_1$  and  $A_2$  are the model parameters,  $y_i$  is the prediction for the  $i$ th atom, and  $y$  is the final adsorption energy prediction after summing over all atoms (denoted by  $i$ ). No bias terms are needed. The activation function  $f$  is chosen to be hyperbolic tangent. The model parameters ( $A_1$  and  $A_2$ ) are shared for all atoms as opposed to having different sets of parameters for different atoms, making the NN model compact (36 parameters in total), reducing the required training data size, and, most importantly, making it possible to directly observe the contributions from individual metal atoms.

NN training was implemented with the Python package tensorflow, using the back-propagation method<sup>70</sup> and using mean-square error as the loss function. Parameter optimization was done using the Adam optimizer with a learning rate of 0.0001. Convergence is achieved in a maximum of 3,000 epochs (Figure S2). Performance metrics used in this work are the MAE and RMSE, defined as

$$\text{MAE} = \frac{1}{N} \sum_{i=0}^N |y_i - \hat{y}_i|, \quad (\text{Equation 4})$$

$$\text{RMSE} = \sqrt{\frac{1}{N} \sum_{i=0}^N (y_i - \hat{y}_i)^2}, \quad (\text{Equation 5})$$

where  $\hat{y}_i$  and  $y_i$  are the NN-predicted and actual values (adsorption energy) of the  $i$ th data sample, respectively, and  $N$  is the total number of data points.

### SUPPLEMENTAL INFORMATION

Supplemental Information can be found online at <https://doi.org/10.1016/j.matt.2020.07.029>.

### ACKNOWLEDGMENTS

The authors acknowledge funding by the University of Toronto and the Natural Sciences and Engineering Research Council of Canada through the discovery grant and undergraduate scholarship programs. We also acknowledge Compute Canada for providing computing resources at the SciNet, CalculQuebec, and Westgrid consortia.

### AUTHORS CONTRIBUTIONS

Conceptualization, Z.L. and C.V.S.; Methodology, Z.L., Z.W.C., and C.V.S.; Software, Z.L.; Formal Analysis, Z.L.; Investigation, Z.L. and Z.W.C.; Data Curation, Z.L.; Writing – Original Draft, Z.L.; Writing – Review & Editing, Z.L., Z.W.C., and C.V.S.; Visualization, Z.L.; Supervision, C.V.S.; Project Administration, C.V.S.; Funding Acquisition: C.V.S.

## DECLARATION OF INTERESTS

The authors declare no competing interests.

Received: May 4, 2020

Revised: June 26, 2020

Accepted: July 24, 2020

Published: August 18, 2020

## REFERENCES

- George, E.P., Raabe, D., and Ritchie, R.O. (2019). High-entropy alloys. *Nat. Rev. Mater.* 4, 515–534.
- Löffler, T., Savan, A., Garzón-Manjón, A., Meischien, M., Scheu, C., Ludwig, A., and Schuhmann, W. (2019). Toward a paradigm shift in electrocatalysis using complex solid solution nanoparticles. *ACS Energy Lett.* 4, 1206–1214.
- Zhang, G., Ming, K., Kang, J., Huang, Q., Zhang, Z., Zheng, X., and Bi, X. (2018). High entropy alloy as a highly active and stable electrocatalyst for hydrogen evolution reaction. *Electrochim. Acta* 279, 19–23.
- Qiu, H.-J., Fang, G., Gao, J., Wen, Y., Lv, J., Li, H., Xie, G., Liu, X., and Sun, S. (2019). Noble metal-free nanoporous high-entropy alloys as highly efficient electrocatalysts for oxygen evolution reaction. *ACS Mater. Lett.* 1, 526–533.
- Jin, Z., Lv, J., Jia, H., Liu, W., Li, H., Chen, Z., Lin, X., Xie, G., Liu, X., Sun, S., et al. (2019). Nanoporous Al-Ni-Co-Ir-Mo high-entropy alloy for record-high water splitting activity in acidic environments. *Small* 15, 1904180.
- Qiu, H.J., Fang, G., Wen, Y., Liu, P., Xie, G., Liu, X., and Sun, S. (2019). Nanoporous high-entropy alloys for highly stable and efficient catalysts. *J. Mater. Chem. A* 7, 6499–6506.
- Xie, P., Yao, Y., Huang, Z., Liu, Z., Zhang, J., Li, T., Wang, G., Shahbazian-Yassar, R., Hu, L., and Wang, C. (2019). Highly efficient decomposition of ammonia using high-entropy alloy catalysts. *Nat. Commun.* 10, 4011.
- Xia, Z., Li, C.M., and Dai, L. (2019). Controlled surface elemental distribution enhances catalytic activity and stability. *Matter* 1, 1447–1449.
- Bligaard, T., and Nørskov, J.K. (2007). Ligand effects in heterogeneous catalysis and electrochemistry. *Electrochim. Acta* 52, 5512–5516.
- Liu, P., Qin, R., Fu, G., and Zheng, N. (2017). Surface coordination chemistry of metal nanomaterials. *J. Am. Chem. Soc.* 139, 2122–2131.
- Liu, P., and Nørskov, J.K. (2001). Ligand and ensemble effects in adsorption on alloy surfaces. *Phys. Chem. Chem. Phys.* 3, 3814–3818.
- Sanchez, J.M. (1993). Cluster expansions and the configurational energy of alloys. *Phys. Rev. B* 48, 14013–14015.
- Calle-Vallejo, F., Loffreda, D., Koper, M.T.M., and Sautet, P. (2015). Introducing structural sensitivity into adsorption-energy scaling relations by means of coordination numbers. *Nat. Chem.* 7, 403–410.
- Batchelor, T.A.A., Pedersen, J.K., Winther, S.H., Castelli, I.E., Jacobsen, K.W., and Rossmeisl, J. (2019). High-entropy alloys as a discovery platform for electrocatalysis. *Joule* 3, 834–845.
- Yao, Y., Huang, Z., Xie, P., Lacey, S.D., Jacob, R.J., Xie, H., Chen, F., Nie, A., Pu, T., Rehwoldt, M., et al. (2018). Carbothermal shock synthesis of high-entropy-alloy nanoparticles. *Science* 359, 1489–1494.
- Li, S., Tang, X., Jia, H., Li, H., Xie, G., Liu, X., Lin, X., and Qiu, H.J. (2020). Nanoporous high-entropy alloys with low Pt loadings for high-performance electrochemical oxygen reduction. *J. Catal.* 383, 164–171.
- Yang, G., Zhao, Y., Lee, D.H., Park, J.M., Seok, M.Y., Suh, J.Y., Ramamurty, U., and Jang, J. il (2019). Influence of hydrogen on incipient plasticity in CoCrFeMnNi high-entropy alloy. *Scr. Mater.* 161, 23–27.
- Cao, S., Tao, F.F., Tang, Y., Li, Y., and Yu, J. (2016). Size- and shape-dependent catalytic performances of oxidation and reduction reactions on nanocatalysts. *Chem. Soc. Rev.* 45, 4747–4765.
- Calle-Vallejo, F., Martínez, J.I., García-Lastra, J.M., Sautet, P., and Loffreda, D. (2014). Fast prediction of adsorption properties for platinum nanocatalysts with generalized coordination numbers. *Angew. Chem. Int. Ed.* 53, 8316–8319.
- Ulissi, Z.W., Tang, M.T., Xiao, J., Liu, X., Torelli, D.A., Karamad, M., et al. (2017). Machine-learning methods enable exhaustive searches for active bimetallic facets and reveal active site motifs for CO<sub>2</sub> reduction. *ACS Catal.* 7, 6600–6608.
- Saxena, S., Khan, T.S., Jalid, F., Ramteke, M., and Haider, M.A. (2019). In silico high throughput screening of bimetallic and single atom alloys using machine learning and ab initio microkinetic modelling. *J. Mater. Chem. A* 8, 107–123.
- Lu, Z., Yadav, S., and Singh, C.V. (2020). Predicting aggregation energy for single atom bimetallic catalysts on clean and O<sup>+</sup> adsorbed surfaces through machine learning models. *Catal. Sci. Technol.* 10, 86–98.
- Toyao, T., Suzuki, K., Kikuchi, S., Takakusagi, S., Shimizu, K., and Takigawa, I. (2018). Toward effective utilization of methane: machine learning prediction of adsorption energies on metal alloys. *J. Phys. Chem. C* 122, 8315–8326.
- Ma, X., Li, Z., Achenie, L.E.K., and Xin, H. (2015). Machine-learning-augmented chemisorption model for CO<sub>2</sub> electroreduction catalyst screening. *J. Phys. Chem. Lett.* 6, 3528–3533.
- Li, Z., Wang, S., Chin, W.S., Achenie, L.E., and Xin, H. (2017). High-throughput screening of bimetallic catalysts enabled by machine learning. *J. Mater. Chem. A* 5, 24131–24138.
- Xie, C., Niu, Z., Kim, D., Li, M., and Yang, P. (2020). Surface and interface control in nanoparticle catalysis. *Chem. Rev.* 120, 1184–1249.
- Huang, W., and Li, W.X. (2019). Surface and interface design for heterogeneous catalysis. *Phys. Chem. Chem. Phys.* 21, 523–536.
- Wang, X., Li, Z., Qu, Y., Yuan, T., Wang, W., Wu, Y., and Li, Y. (2019). Review of metal catalysts for oxygen reduction reaction: from nanoscale engineering to atomic design. *Chem* 5, 1486–1511.
- Cheng, F., and Chen, J. (2012). Metal-air batteries: from oxygen reduction electrochemistry to cathode catalysts. *Chem. Soc. Rev.* 41, 2172–2192.
- Wang, Z.L., Xu, D., Xu, J.J., and Zhang, X.B. (2014). Oxygen electrocatalysts in metal-air batteries: from aqueous to nonaqueous electrolytes. *Chem. Soc. Rev.* 43, 7746–7786.
- Kulkarni, A., Siahrostami, S., Patel, A., and Nørskov, J.K. (2018). Understanding catalytic activity trends in the oxygen reduction reaction. *Chem. Rev.* 118, 2302–2312.
- Nørskov, J.K., Rossmeisl, J., Logadottir, A., Lindqvist, L., Kitchin, J.R., Bligaard, T., and Jónsson, H. (2004). Origin of the overpotential for oxygen reduction at a fuel-cell cathode. *J. Phys. Chem. B* 108, 17886–17892.
- Chaves, A.S., Piotrowski, M.J., Guedes-Sobrinho, D., and Da Silva, J.L.F. (2015). Theoretical investigation of the adsorption properties of CO, NO, and OH on monometallic and bimetallic 13-atom clusters: the example of Cu<sub>13</sub>, Pt<sub>7</sub>Cu<sub>6</sub>, and Pt<sub>13</sub>. *J. Phys. Chem. A* 119, 11565–11573.
- Zhang, W., Zhu, J., Cheng, D., and Zeng, X.C. (2020). PtCoNi alloy nanoclusters for synergistic catalytic oxygen reduction reaction. *ACS Appl. Nano Mater.* 3, 2536–2544.
- Panayotov, D.A., and Morris, J.R. (2016). Surface chemistry of Au/TiO<sub>2</sub>: thermally and photolytically activated reactions. *Surf. Sci. Rep.* 71, 77–271.

36. Falsig, H., Shen, J., Khan, T.S., Guo, W., Jones, G., Dahl, S., and Bligaard, T. (2014). On the structure sensitivity of direct NO decomposition over low-index transition metal facets. *Top. Catal.* 57, 80–88.
37. Chen, Y., Huang, Y., Cheng, T., and Goddard, W.A. (2019). Identifying active sites for CO<sub>2</sub> reduction on dealloyed gold surfaces by combining machine learning with multiscale simulations. *J. Am. Chem. Soc.* 141, 11651–11657.
38. Pedersen, J.K., Batchelor, T.A.A., Bagger, A., and Rossmeisl, J. (2020). High-entropy alloys as catalysts for the CO<sub>2</sub> and CO reduction reactions. *ACS Catal.* 10, 2169–2176.
39. Schlexer Lamoureaux, P., Winther, K.T., Garrido Torres, J.A., Streibel, V., Zhao, M., Bajdich, M., Abild-Pedersen, F., and Bligaard, T. (2019). Machine learning for computational heterogeneous catalysis. *ChemCatChem* 11, 3581–3601.
40. Xie, T., and Grossman, J.C. (2018). Crystal graph convolutional neural networks for an accurate and interpretable prediction of material properties. *Phys. Rev. Lett.* 120, 145301.
41. Chen, C., Ye, W., Zuo, Y., Zheng, C., and Ong, S.P. (2019). Graph networks as a universal machine learning framework for molecules and crystals. *Chem. Mater.* 31, 3564–3572.
42. Back, S., Yoon, J., Tian, N., Zhong, W., Tran, K., and Ulissi, Z.W. (2019). Convolutional neural network of atomic surface structures to predict binding energies for high-throughput screening of catalysts. *J. Phys. Chem. Lett.* 10, 4401–4408.
43. Behler, J., and Parrinello, M. (2007). Generalized neural-network representation of high-dimensional potential-energy surfaces. *Phys. Rev. Lett.* 98, 146401.
44. Behler, J. (2011). Atom-centered symmetry functions for constructing high-dimensional neural network potentials. *J. Chem. Phys.* 134, 074106.
45. Bartók, A.P., Kondor, R., and Csányi, G. (2013). On representing chemical environments. *Phys. Rev. B Condens. Matter Mater. Phys.* 87, 184115.
46. De, S., Bartók, A.P., Csányi, G., and Ceriotti, M. (2016). Comparing molecules and solids across structural and alchemical space. *Phys. Chem. Chem. Phys.* 18, 13754–13769.
47. Jinnouchi, R., and Asahi, R. (2017). Predicting catalytic activity of nanoparticles by a DFT-aided machine-learning algorithm. *J. Phys. Chem. Lett.* 8, 4279–4283.
48. Jäger, M.O.J., Morooka, E.V., Federici Canova, F., Himanen, L., and Foster, A.S. (2018). Machine learning hydrogen adsorption on nanoclusters through structural descriptors. *NPJ Comput. Mater.* 4, 37.
49. Yan, Y., Zhan, F., Du, J., Jiang, Y., Jin, C., Fu, M., Zhang, H., and Yang, D. (2015). Kinetically-controlled growth of cubic and octahedral Rh-Pd alloy oxygen reduction electrocatalysts with high activity and durability. *Nanoscale* 7, 301–307.
50. Zhu, J., Elnabawy, A.O., Lyu, Z., Xie, M., Murray, E.A., Chen, Z., Jin, W., Mavrikakis, M., and Xia, Y. (2019). Facet-controlled Pt-Ir nanocrystals with substantially enhanced activity and durability towards oxygen reduction. *Mater. Today* 35, 69–77.
51. Liu, Y., Liu, S., Che, Z., Zhao, S., Sheng, X., Han, M., and Bao, J. (2016). Concave octahedral Pd@PdPt electrocatalysts integrating core-shell, alloy and concave structures for high-efficiency oxygen reduction and hydrogen evolution reactions. *J. Mater. Chem. A* 4, 16690–16697.
52. Fu, G., Wu, K., Lin, J., Tang, Y., Chen, Y., Zhou, Y., and Lu, T. (2013). One-pot water-based synthesis of Pt-Pd alloy nanoflowers and their superior electrocatalytic activity for the oxygen reduction reaction and remarkable methanol-tolerant ability in acid media. *J. Phys. Chem. C* 117, 9826–9834.
53. Kim, D.H., Lee, E., and Pak, C. (2019). Effect of rare-earth elements in Pd ternary alloy catalysts on activity toward oxygen reduction reaction. *Catal. Today*, In press. <https://doi.org/10.1016/j.cattod.2019.12.022>.
54. Westsson, E., Picken, S., and Koper, G. (2019). The effect of lattice strain on catalytic activity. *Chem. Commun. (Camb.)* 55, 1338–1341.
55. Khorshidi, A., Violet, J., Hashemi, J., and Peterson, A.A. (2018). How strain can break the scaling relations of catalysis. *Nat. Catal.* 1, 263–268.
56. Zhu, S., Hu, X., and Shao, M. (2017). Impacts of anions on the oxygen reduction reaction kinetics on platinum and palladium surfaces in alkaline solutions. *Phys. Chem. Chem. Phys.* 19, 7631–7641.
57. Liu, J., and Huang, Y. (2018). Oxygen reduction reaction on PtCo nanocatalyst: (Bi)sulfate anion poisoning. *Nanoscale Res. Lett.* 13, 156.
58. Calle-Vallejo, F., Tymoczko, J., Colic, V., Vu, Q.H., Pohl, M.D., Morgenstern, K., Loffreda, D., Sautet, P., Schuhmann, W., and Bandarenka, A.S. (2015). Finding optimal surface sites on heterogeneous catalysts by counting nearest neighbors. *Science* 350, 185–189.
59. Xia, B.Y., Wu, H.B., Wang, X., and Lou, X.W. (2013). Highly concave platinum nanoframes with high-index facets and enhanced electrocatalytic properties. *Angew. Chem. Int. Ed.* 52, 12337–12340.
60. Kresse, G., and Furthmüller, J. (1996). Efficient iterative schemes for ab initio total-energy calculations using a plane-wave basis set. *Phys. Rev. B Condens. Matter Mater. Phys.* 54, 11169–11186.
61. Blöchl, P.E. (1994). Projector augmented-wave method. *Phys. Rev. B* 50, 17953–17979.
62. Perdew, J.P., Burke, K., and Ernzerhof, M. (1996). Generalized gradient approximation made simple. *Phys. Rev. Lett.* 77, 3865–3868.
63. Stöhr, M., Van Voorhis, T., and Tkatchenko, A. (2019). Theory and practice of modeling van der Waals interactions in electronic-structure calculations. *Chem. Soc. Rev.* 48, 4118–4154.
64. Su, G., Yang, S., Li, S., Butch, C.J., Filimonov, S.N., Ren, J.C., and Liu, W. (2019). Switchable Schottky contacts: simultaneously enhanced output current and reduced leakage current. *J. Am. Chem. Soc.* 141, 1628–1635.
65. Grimme, S., Antony, J., Ehrlich, S., and Krieg, H. (2010). A consistent and accurate ab initio parametrization of density functional dispersion correction (DFT-D) for the 94 elements H–Pu. *J. Chem. Phys.* 132, 154104.
66. Hjorth Larsen, A., Jørgen Mortensen, J., Blomqvist, J., Castelli, I.E., Christensen, R., Dufak, M., Friis, J., Groves, M.N., Hammer, B., Hargus, C., et al. (2017). The atomic simulation environment - a Python library for working with atoms. *J. Phys. Condens. Matter* 29, 273002.
67. Tran, R., Xu, Z., Radhakrishnan, B., Winston, D., Sun, W., Persson, K.A., et al. (2016). Surface energies of elemental crystals. *Sci. Data* 3, 160080.
68. Roling, L.T., Choksi, T.S., and Abild-Pedersen, F. (2019). A coordination-based model for transition metal alloy nanoparticles. *Nanoscale* 11, 4438–4452.
69. Li, Y., and Guo, W. (2019). Machine-learning model for predicting phase formations of high-entropy alloys. *Phys. Rev. Mater.* 3, 095005.
70. Rumelhart, D.E., Hinton, G.E., and Williams, R.J. (1986). Learning representations by back-propagating errors. *Nature* 323, 533–536.

**Matter, Volume 3**

**Supplemental Information**

**Neural Network-Assisted Development  
of High-Entropy Alloy Catalysts: Decoupling  
Ligand and Coordination Effects**

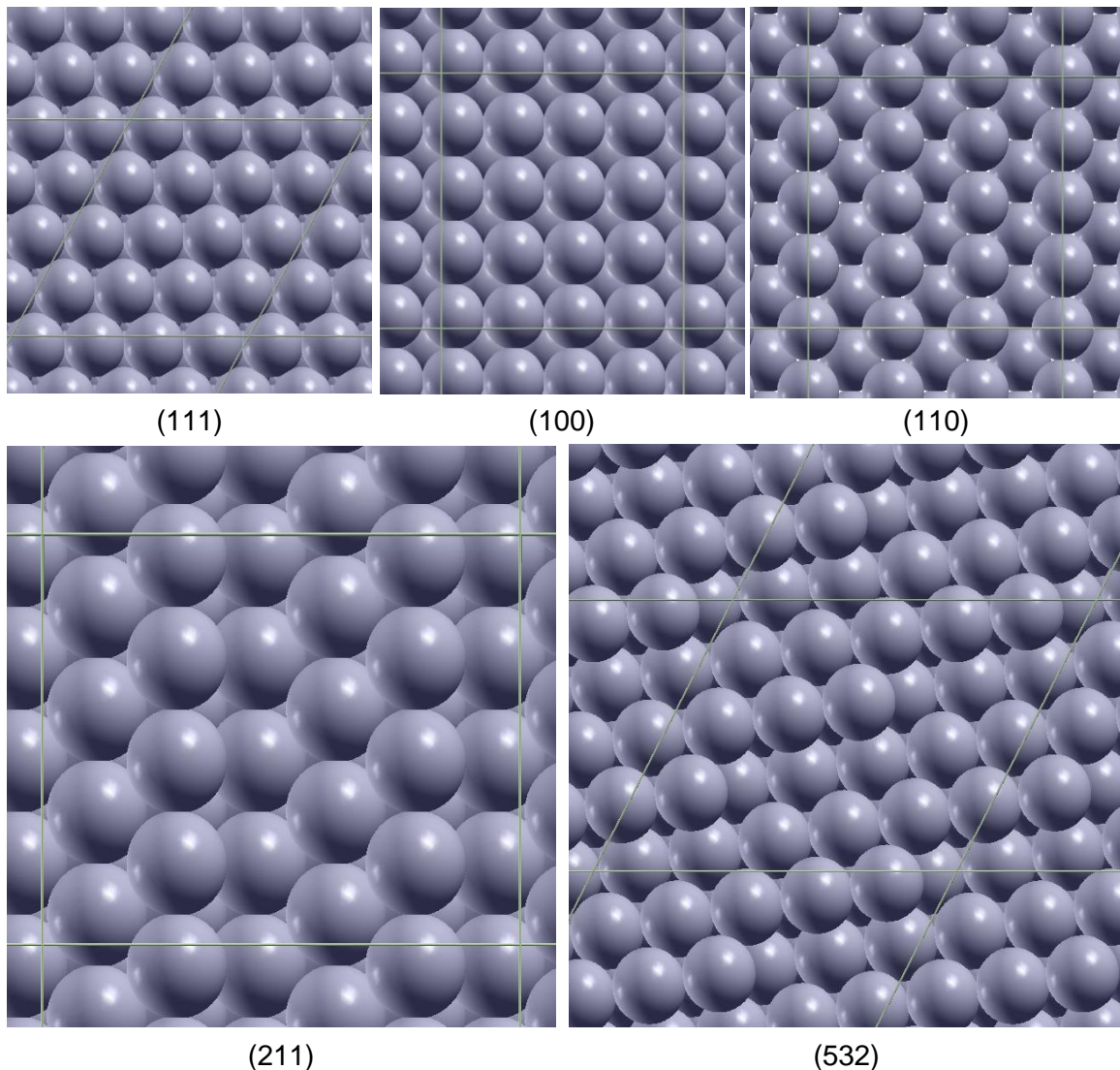
**Zhuole Lu, Zhi Wen Chen, and Chandra Veer Singh**

## Supplemental Data Items

### 1. Surface models

Top views of the surface models used in this work, corresponding to Figure 1 in main text, are shown in Figure S1.

Figure S1. Top views of surface models used in this study, corresponding to the side views in Figure 1 in main text.



### 2. Trained weights of NN

Sample trained NN weights are given below. Note that before NN training, the group number, period number and atomic radii were first normalized by subtracting these values from those of Ru. So in order to use these weights directly, one needs to first reference the group number, period number and atomic radii (in pm) with respect to Ru. In other words, use Ru: 0,0,0, Rh: 0,1,0, Pd: 0,2,3, Ir: 1,1,1.5, Pt: 1,2,4.5.

Note there are 30 parameters in first NN layer and 6 in second, giving 36 in total.

First NN layer:

```

[-0.192935, -2.128473, -0.5890434, -0.23783036, -1.0142646, -0.01790326],
[ 0.486281, -0.2363347, 1.713717, -0.66623807, -0.8341955, 0.14510955],
[ 0.3745039, -0.8992171, 0.26786217, 0.20112726, 0.7327471, 0.50042224],
[-0.392292, 0.6304792, 0.15683521, 0.21771273, 0.3118519, -0.35696217],
[-0.2945569, -3.8742847, -2.6877038, -1.4017274, -0.6213934, -0.60586584]],

```

Second NN layer:

```

[[ 0.74206084],
[-0.04996059],
[ 0.42490107],
[ 0.7585831 ],
[-0.7749046 ],
[-0.5185522 ]]

```

### 3. Coordination numbers of surface models used in this work

Table S1. Coordination numbers of surface models used in this work, as depicted in Figure 1.

Active site atoms	Nearest neighbours														
	9	9	9	9	9	9	9	9	9	12	12	12	12	12	
9-9 (111)	9	9	9	9	9	9	9	9	9	12	12	12	12	12	
8-8 (100)	8	8	8	8	8	8	12	12	12	12	12	12	12	12	
7-7 (110)	7	7	7	7	11	11	11	11	11	11	12	12	12	12	
7-7 (211)	7	7	7	7	9	9	9	12	12	12	13	13	13	13	
7-10 (211)	7	10	7	7	9	9	9	9	10	10	10	12	12	12	12
9-10 (211)	9	10	7	7	7	9	9	10	10	12	12	12	12	12	12
6-7 (532)	6	7	12	12	9	9	8	11	10	10	8				
6-8 (532)	6	8	12	10	7	9	11	12	12	10	9	7			
7-8 (532)	7	8	9	9	6	12	12	10	11	6	9	10	12		
7-10 (532)	7	10	8	9	9	6	12	12	11	9	9	10	12	12	
6-10 (532)	6	10	7	9	8	12	11	10	9	8	9	12	12	12	
8-10 (532)	8	10	6	12	10	11	9	9	6	7	12	12	12	12	11

### 4. Training curve

We show how NN is iterative trained to approach its maximal accuracy using the training curve shown in Figure S2. The majority of training is done within the first 1000 epochs, and limited improvement is observed beyond 2000 epochs.

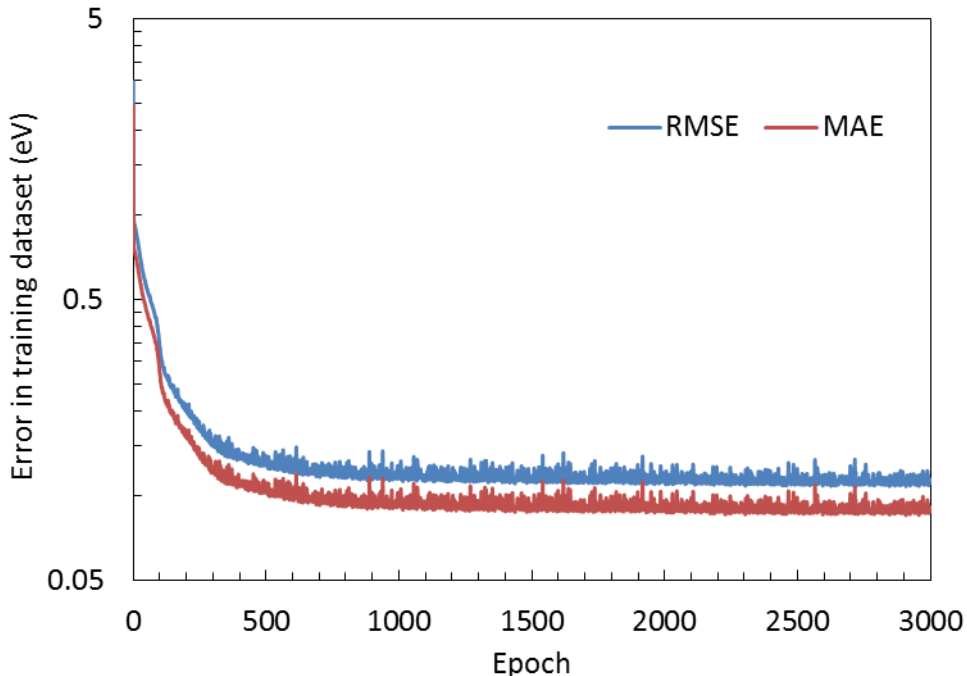


Figure S2. Training curve of NN model referenced in neural network description in main text.

### 5. Conversion between calculated electronic energy ( $E$ ) and free energy ( $G$ )

This work assumes the associative mechanism of ORR where the elementary steps follow

- (1)  $O_2 + (H^+ + e^-) \rightarrow *OOH$
- (2)  $*OOH + (H^+ + e^-) \rightarrow *O + H_2O$
- (3)  $*O + (H^+ + e^-) \rightarrow *OH$
- (4)  $*OH + (H^+ + e^-) \rightarrow H_2O$

and the potential limiting is either the initial or final steps.<sup>1</sup>

The theoretical overpotential is, therefore,

$$U_L = \max(\Delta G_{OOH}, -\Delta G_{OH})$$

where  $\Delta G$  is the free energy of each elementary step.  $\Delta G$  is related to the calculated electronic energy,  $\Delta E$ , as  $\Delta G = \Delta E + ZPE + T\Delta S$ , where ZPE is the zero-point energy correction,  $T$  is the temperature, and  $\Delta S$  is the change in entropy corresponding to the elementary step.

To convert from  $\Delta E$ , which is the quantity predicted by the NN model in this work, to  $\Delta G$ , we use the approximation  $\Delta G_{OH} = \Delta E_{OH} + 0.35$  eV which was established by previous work.<sup>2</sup> This approximation hinges on the fact that the ZPE and entropy correction do not vary much across different metallic surfaces, even when the surface coordination varies.<sup>3</sup> To obtain  $\Delta G_{OOH}$ , we used  $\Delta G_{OOH} = \Delta G_{OH} + 3.2$  eV as established by linear scaling relationship.<sup>1</sup>

### 6. Data for experimental validation

In Experimental Validation section of the main text, the activity measurements of all studies were conducted at mostly identical conditions, including temperature, electrolyte, and scan rate, and therefore values can be compared fairly. Additionally, all referenced studies were ensured that either the studied catalyst is well-mixed solid solution or at least top two atomic layers are well-mixed solid solution (as opposed to, for example, core-shell structures where the surface has one element only), as the NN model assumes random distribution of all elements. Lastly, measurements where one component's molar ratio is lower than 20% are excluded, since such samples are significantly inconsistent the near-equimolar requirement of HEAs.

For making predictions of the adsorption energy values of the data points in Figure 7, all predictions are made on a fully-trained NN model using all data points available, as also for the case of Figures 3-5. For cubes, the average value of the full adsorption energy distribution on 8-8 (100) sites is taken. For octahedra, the average value of the full adsorption energy distribution on 9-9 (111) and 9-10 (211) sites is taken, because, as pointed out in the referenced papers, the synthesized octahedra possess concave structures, so 9-10 (211) (which is a concave site) is added on top of 9-9 (111) to reflect the presence of these concave sites. The only mixed (cubo-octahedron) site is the Pt point, serving as a reference material. Its adsorption energy is taken as the average value of the full adsorption energy distribution on 9-9 (111) and 8-8 (100) sites.

## 7. Van der Waals correction

We test the effect of van der Waals (vdW) correction on DFT data by randomly selecting 25 data points from the dataset and compare DFT-calculated OH\* adsorption energy values with and without vdW correction. To account for vdW interactions, Grimme's DFT-D3 method was used.<sup>4</sup> The results are shown in Figure S3. Note that this comparison was directly made on the final model output, i.e. the OH\* adsorption energy referenced to Pt(111),  $\Delta E_{\text{OH}} - \Delta E_{\text{OH},\text{Pt}(111)}$ . Linear regression shows a slope near 1 and an intercept near 0, indicating that vdW correction yields negligible change to the dataset output variable. Furthermore, the residual values,  $[\Delta E_{\text{OH}} - \Delta E_{\text{OH},\text{Pt}(111)}]_{\text{without VdW}} - [\Delta E_{\text{OH}} - \Delta E_{\text{OH},\text{Pt}(111)}]_{\text{with VdW}}$ , have an average value of 0.03 eV and a standard deviation of 0.07 eV, which are consistent the ~0.12 eV RMSE of the NN model. This is possibly due to the cancellation of vdW effects when all calculations were made in reference to Pt(111). Therefore, vdW correction was not used for generating the dataset.

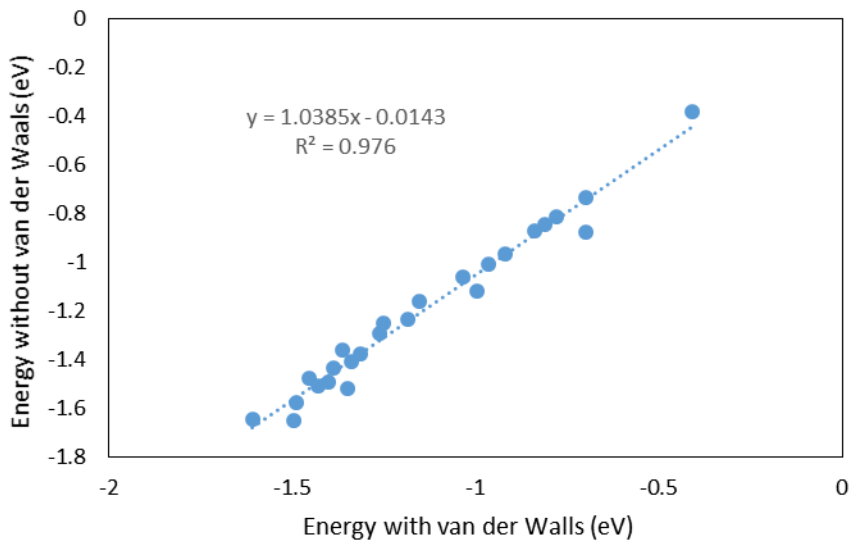


Figure S3. Comparison between DFT-calculated adsorption energy ( $\Delta E_{\text{OH}} - \Delta E_{\text{OH},\text{Pt}(111)}$ ) with and without van der Waals corrections.

## 8. Data and code availability

The data and code necessary for examining the NN architecture and for reproducing figures in this work are publically available at online repository: <https://github.com/jol-jol/neural-network-design-of-HEA>. The data is also presented in the attached csv file "HEA\_data.csv", in more compact form. In "HEA\_data.csv" file, each line contains a new HEA structure, and the format of each line is as follows: name\_of\_surface\_type, name\_of\_active\_site\_type, element\_of\_atom\_1, CN\_of\_atom\_1, element\_of\_atom\_2, CN\_of\_atom\_2, element\_of\_atom\_3, CN\_of\_atom\_3, ..., element\_of\_atom\_N, CN\_of\_atom\_N, adsorption\_energy\_OH\_relative\_to\_Pt(111)

## Supplemental References

1. Kulkarni, A., Siahrostami, S., Patel, A., and Nørskov, J.K. (2018). Understanding catalytic activity trends in the oxygen reduction reaction. *Chem. Rev.* **118**, 2302–2312.
2. Nørskov, J.K., Rossmeisl, J., Logadottir, A., Lindqvist, L., Kitchin, J.R., Bligaard, T., and Jónsson, H. (2004). Origin of the overpotential for oxygen reduction at a fuel-cell cathode. *J. Phys. Chem. B* **108**, 17886–17892.
3. Herron, J.A., Jiao, J., Hahn, K., Peng, G., Adzic, R.R., and Mavrikakis, M. (2012). Oxygen reduction reaction on platinum-terminated “onion-structured” alloy catalysts. *Electrocatalysis* **3**, 192–202.
4. Grimme, S., Antony, J., Ehrlich, S., and Krieg, H. (2010). A consistent and accurate ab initio parametrization of density functional dispersion correction (DFT-D) for the 94 elements H-Pu. *J. Chem. Phys.* **132**, 154104.